

Discovery and Manipulation of van der Waals Polarons in Sb₂O₃ Ultrathin Molecular Crystal

Zhi-Hao Zhang,[#] Linlu Wu,[#] Mao-Peng Miao, Hao-Jun Qin, Gang Chen, Min Cai, Lixin Liu, Lan-Fang Zhu, Wenhao Zhang, Tianyou Zhai, Wei Ji,^{*} and Ying-Shuang Fu^{*}



Cite This: <https://doi.org/10.1021/jacs.4c04450>



Read Online

ACCESS |



Metrics & More

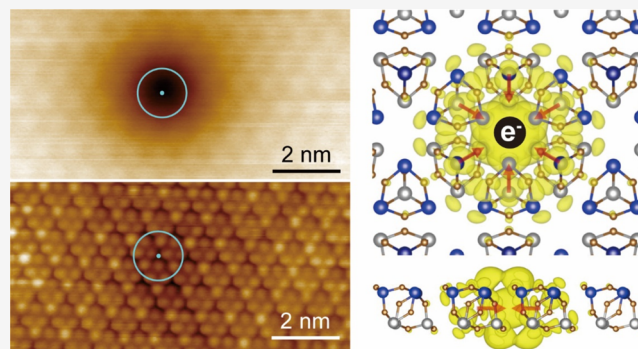


Article Recommendations



Supporting Information

ABSTRACT: Manipulating single electrons at the atomic scale is vital for mastering complex surface processes governed by the transfer of individual electrons. Polarons, composed of electrons stabilized by electron–phonon coupling, offer a pivotal medium for such manipulation. Here, using scanning tunneling microscopy and spectroscopy (STM/STS) and density functional theory (DFT) calculations, we report the identification and manipulation of a new type of polaron, dubbed van der Waals (vdW) polaron, within mono- to trilayer ultrathin films composed of Sb₂O₃ molecules that are bonded via vdW attractions. The Sb₂O₃ films were grown on a graphene-covered SiC(0001) substrate via molecular beam epitaxy. Unlike prior molecular polarons, STM imaging observed polarons at the interstitial sites of the molecular film, presenting unique electronic states and localized band bending. DFT calculations revealed the lowest conduction band as an intermolecular bonding state, capable of ensnaring an extra electron through locally diminished intermolecular distances, thereby forming an intermolecular vdW polaron. We also demonstrated the ability to generate, move, and erase such vdW polarons using an STM tip. Our work uncovers a new type of polaron stabilized by coupling with intermolecular vibrations where vdW interactions dominate, paving the way for designing atomic-scale electron transfer processes and enabling precise tailoring of electron-related properties and functionalities.



INTRODUCTION

The manipulation of individual atoms and molecules on surfaces represents a “quantum” leap in nanotechnology, laying the groundwork for atomic-precision engineering of material properties and the realization of novel quantum nanostructures.^{1–4} Extending such manipulation ability to individual electrons is desirable in view that electron transfer is essential for various chemical processes.⁵ Nevertheless, the manipulation of single electrons is subtle and less straightforward, as the motion of single electrons is fully governed by the laws of quantum mechanics. Previous endeavors toward manipulating single electrons include an electrostatic approach of controlling the charge state of single atoms or molecules on insulators.^{6–8} Alternatively, the scanning tunneling microscopy (STM)-tip-induced band bending effect was implemented to control the charge states of donors or acceptors in semiconductors.^{9–11} However, those methods rely on specific properties of the atomic species, which also limit the type of residing sites of electrons.

Polarons, comprised of electrons stabilized by local lattice distortion through electron–phonon coupling,^{12,13} offer an ideal medium for the manipulation of single electrons.^{14,15} In particular, small polaron, localized by confined short-range

electron–phonon coupling,^{15,16} induces local lattice distortions typically in sizes of one atomic lattice period, enabling its manipulation onto desired locations with atomic precision. Polarons play a significant role in various areas of chemistry, influencing charge transport, redox reactions, catalysis, molecular structure, and energy storage.^{5,8,17–22} Thus, studying single polarons, apart from controlling single electrons, is also pivotal for understanding the mechanism governing the aforementioned chemical processes.

Polarons are dominantly hosted in material systems bonded by covalent or ionic interactions, such as transition metal oxides, halides, perovskites, and organic polymers.^{23–31} Recently, noncovalent interactions, e.g., dispersion attraction and Pauli repulsion, have been found to offer strong electronic^{32,33} and vibrational³⁴ couplings across van der Waals (vdW) gaps. Such a combination of interactions was

Received: March 31, 2024

Revised: June 19, 2024

Accepted: June 21, 2024

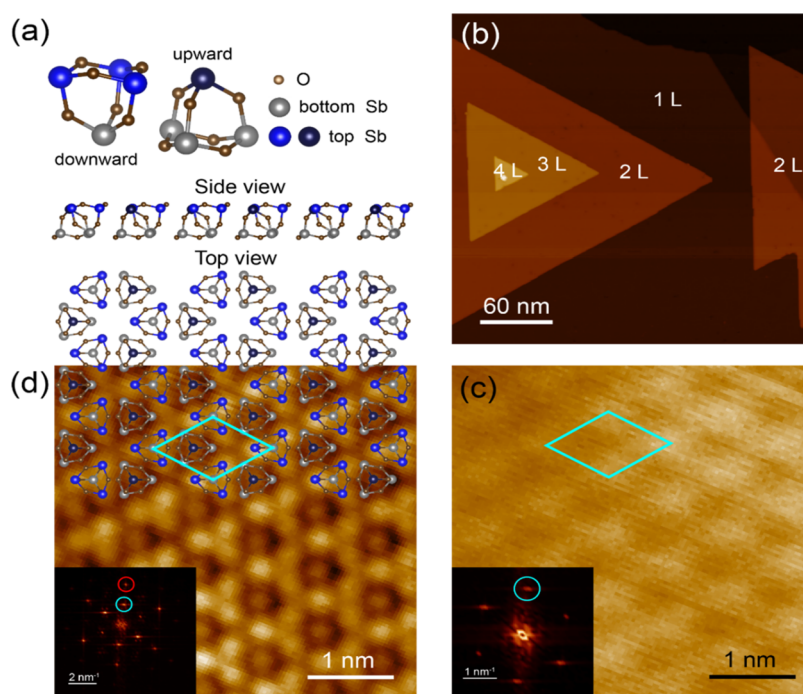


Figure 1. Structure and morphology of α - Sb_2O_3 thin films. (a) Ball-and-stick structural models of upward- and downward-oriented Sb_4O_6 molecular cages and the side and top views of the crystal structure of monolayer α - Sb_2O_3 . (b) Large-area STM image ($V_s = 3$ V, $I_t = 5$ pA) showing the topography of α - Sb_2O_3 thin films grown on a graphene substrate. (c, d) High-resolution STM images of the α - Sb_2O_3 film at the same region taken with different imaging conditions [$V_s = 2.5$ V, $I_t = 10$ pA for (c); $V_s = 2.0$ V, $I_t = 10$ pA for (d)]. Insets are the associated FFT images, where reciprocal spots for the top-layer Sb lattice and the unit lattice are marked with red and azure circles, respectively. The real-space lattice unit is marked with an azure rhombus in (c, d).

termed quasi-bonding.³⁵ It is of fundamental significance to explore whether excess electrons can be stabilized by such quasibonds existing within vdW gaps, generating polarons.

Here, using STM, we report the observation and manipulation of single polarons involving noncovalent interactions in Sb_2O_3 molecular crystals grown on graphene-covered SiC(0001). Individual polarons were identified to occupy the interstitial lattice site of the Sb_2O_3 molecular crystal, exhibiting polaronic states and local upward band bending. We demonstrated the capability of creation, movement, and erasure of individual single polarons in a controlled fashion with an electric field exerted from the STM tip. Density functional theory (DFT) calculations unveiled that an excess electron occupies an intermolecular bonding state and shortens the intermolecular distance locally, although the intermolecular attraction is dominated by the vdW interactions. Such strong coupling of the electron with the local lattice stabilizes the excess electron, forming a dubbed vdW polaron. Our study uncovers a polaron type and provides a feasible route to manipulate individual electrons at the atomic scale.

The experiments were performed with a custom-made Unisoku STM system (1500) at 4.2 K.³⁶ The Sb_2O_3 films were grown by molecular beam epitaxy (MBE) on a graphene substrate. First-principles calculations were carried out with the DFT approach. The detailed methods are depicted in the Methods Section.

RESULTS AND DISCUSSION

Antimony trioxide (Sb_2O_3) solid is an inorganic molecular crystal, composed of Sb_4O_6 polyhedral cages that are bonded to each other through vdW interactions. The α -phase Sb_2O_3 crystal is cubic and belongs to the $Fd\bar{3}m$ space group,³⁷ where

its Sb_4O_6 cages are alternately stacked in upward- and downward orientations, forming two sets of regular triangular lattice [Figure 1a]. Figure 1b displays a typical topographic image of the as-grown α - Sb_2O_3 thin films, showing regular triangular shapes with straight step edges. The Sb_2O_3 films grow continuously across the step edges of graphene, suggesting that the binding energy of the molecular cages attached to the side is lower than that attached to the surface. The phase structure of α - Sb_2O_3 thin films has been well-characterized via Raman spectra and X-ray diffraction measurements previously.^{38,39} Upon imaging the film with a bias beyond the insulating gap at 3.0 V, the apparent monolayer height of the second layer of Sb_2O_3 is 6.4 Å [Figure S1], which is close to the actual height measured with X-ray diffraction,⁴⁰ and also agrees with our measurement with an atomic force microscope [Figure S2].

An atomic-resolution STM image [Figure 1c] acquired at 2.5 V and its associated fast Fourier transform (FFT) image [Figure 1c, inset] clearly indicate a triangular lattice of up-down pairs of Sb_4O_6 molecular cages. The measured lattice constant is 7.86 Å, consistent with the X-ray measured value of 7.89 Å.⁴⁰ Decreasing the bias voltage to 2.0 V, a typical STM image of the same Sb_2O_3 area reveals the top-layer Sb atoms [Figure 1d] in two categories with apparent height. In such an image, each Sb_2O_3 pair contains four visible top-layer Sb atoms, among which one appears more depressed than the other three, as assigned to the upward- and downward-oriented Sb_4O_6 molecular cages, respectively. Multiple moiré patterns were revealed in the Sb_2O_3 monolayer as a result of different relative angles between Sb_2O_3 films and graphene substrates [Figure S3].

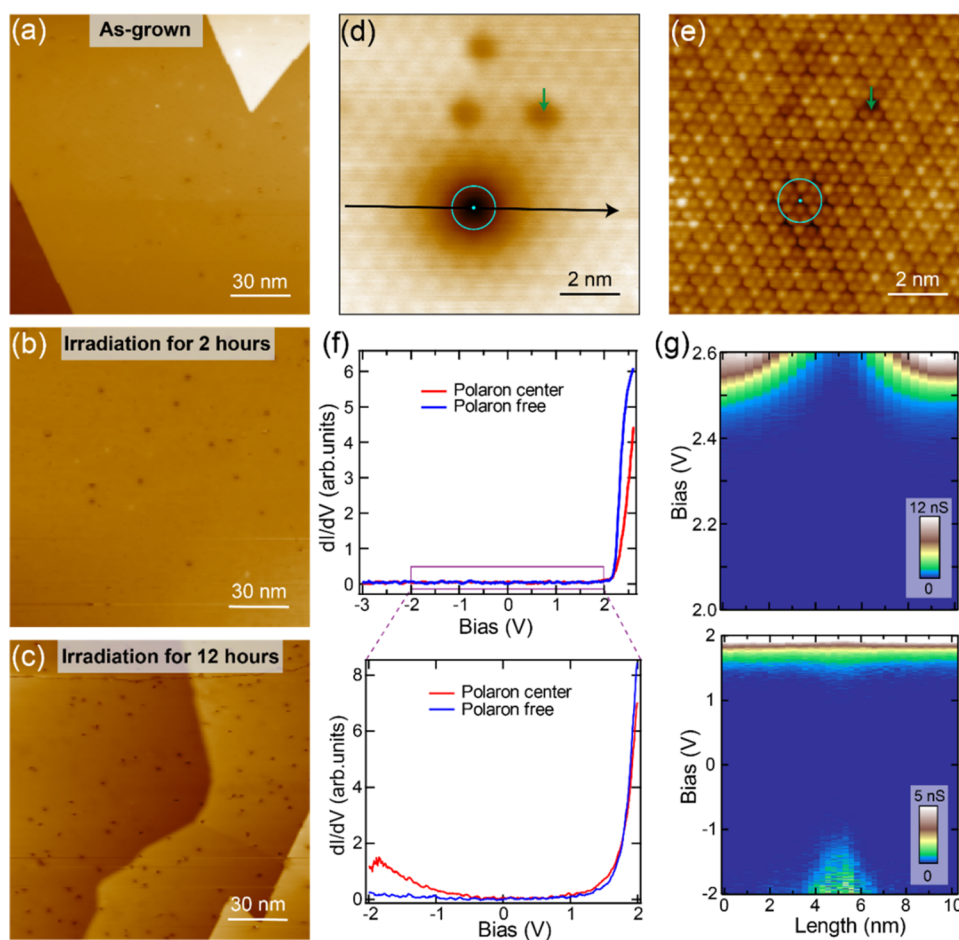


Figure 2. Characterization of depressed entities. (a–c) Large-scale STM topographic images ($V_s = 3$ V, $I_t = 10$ pA) of as-grown (a) Sb_2O_3 films and their decorated depressed entities after electron irradiation for 2 h (b) and 12 h (c), respectively. The images in parts (a–c) are mainly on the first layer Sb_2O_3 . (d, e) Atomic resolution images of depressed entities in the same area on the second layer Sb_2O_3 with different imaging conditions ($V_s = 3$ V, $I_t = 10$ pA for (d); $V_s = 2.0$ V, $I_t = 10$ pA for (e)). The green arrows indicate the intrinsic dark triangle defects and are adopted as the marks; the azure circles are guided for the eye showing the spatial extensions of depressed entities. (f) dI/dV spectra acquired on the entity center (red) and entity-free area (blue) of Sb_2O_3 thin films (set point: $V_s = +2.6$ V, $I_t = 100$ pA, $V_{\text{mod}} = 60$ mV). The lower panel shows the dI/dV spectra within the zoom-in bias range. (g) 2D conductance plots of the depressed entity taken along the black line in (d) with different energy intervals. Spectroscopic conditions: $V_s = +2.6$ V, $I_t = 50$ pA, $V_{\text{mod}} = 30$ mV for the upper panel; $V_s = +2$ V, $I_t = 50$ pA, $V_{\text{mod}} = 40$ mV for the lower panel.

On the as-grown Sb_2O_3 film shown in Figure 2a, there were some depressed entities observable on the surface. We found such entities could be generated upon irradiating the as-grown film with electrons emitted from a filament in the ultrahigh vacuum chamber, whose details are depicted in the Methods Section. The density of these depressed entities increased after electron irradiation for 2 h [Figure 2b] and continuously and monotonically enlarged with prolonged electron irradiation time up to 12 h [Figure 2c]. The density of entities after electron beam radiation is similar for the monolayer and bilayer film [Figure S4], demonstrating that the influence of the substrate is negligible.

We scrutinized the nature of the depressed entities. Figure 2d shows a typical STM image of a depressed entity appearing as a circular depression. Its appearance changes noticeably with imaging bias, whose radius decreases gradually with increasing bias voltage from 2.5 to 3 V and becomes invisible below 2.4 V [Figure S5]. High-resolution STM imaging of the depressed entities determines their occupation sites. By comparing the STM images in Figure 2d,e, we could clearly identify that the entity is centered at the interstitial site of the molecular units, as marked by the azure dots, without detectable local lattice

distortions around the entity. Besides, there exists another type of depressed entity centered on top of the molecular unit [Figure S6], but such entities are very rare and not discussed hereafter. There are two types of commonly observed intrinsic defects in the Sb_2O_3 films that appear as dark triangular [Figure 2d, marked with green arrows] and clover-shapes [Figure S7] defects. They are located on the O sites of the downward- and upward-oriented Sb_4O_6 cages, respectively, and are thus both ascribed as the O vacancies. Those defects do not show observable perturbations to the local density of states of the film [Figure S8] and are distinct from the depressed entities in morphology and electronic character.

Next, the electronic properties of the depressed entities were measured with STS [Figure 2d]. The tunneling spectra of the clean Sb_2O_3 film indicate its conduction band minimum (CBM) located at about 2 eV [Figure 2f] that is spatially uniform [Figure S9]. Its valence band maximum (VBM) is below the measured spectral range of -3 eV, indicating that its band gap is larger than 5 eV. This gap value is in line with that measured by optical methods of 5.6 eV.⁴¹ The tunneling spectra of the entities, on the other hand, noticeably modify the local density of states (LDOS) [Figure 2f,g]. A two-

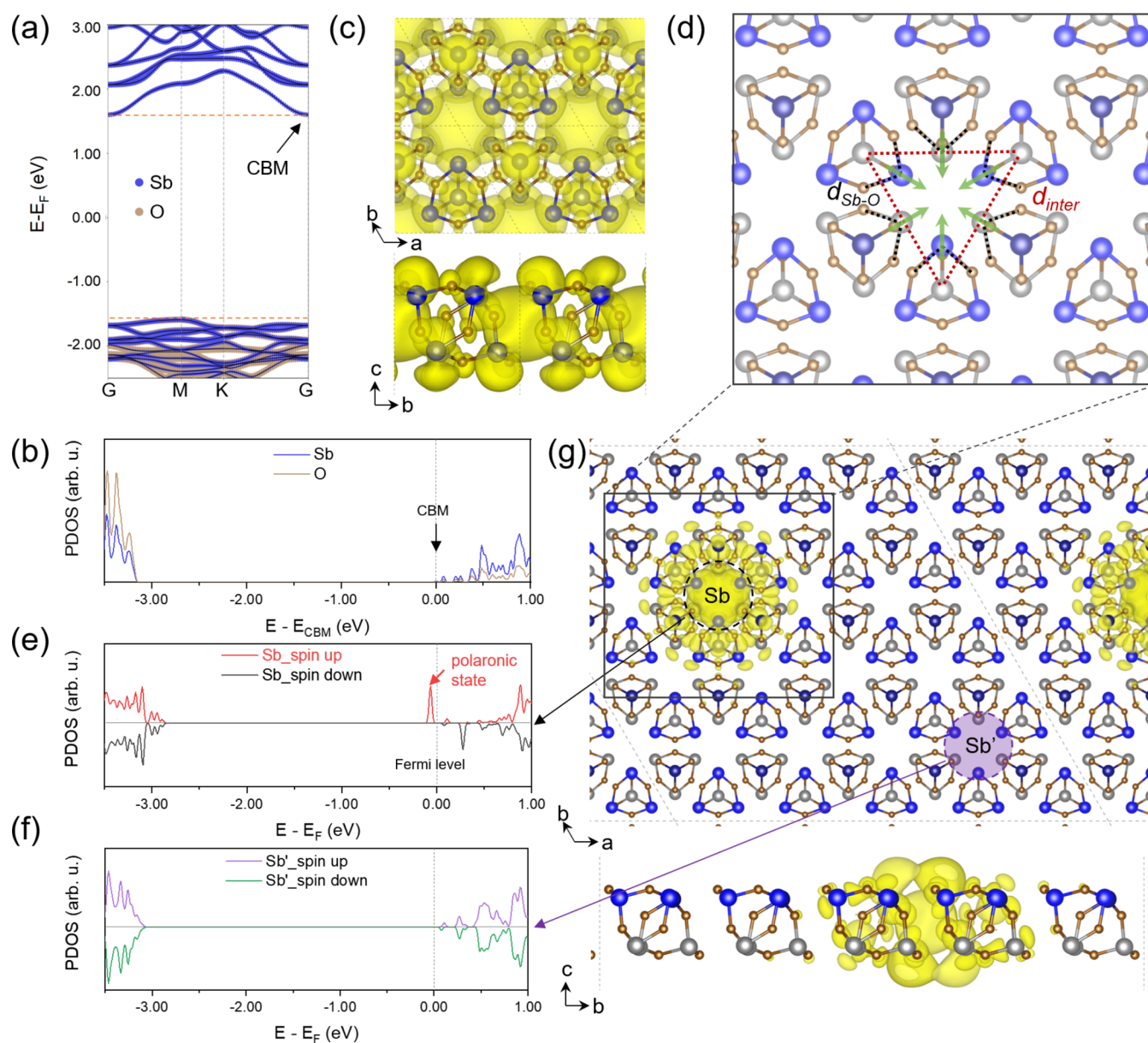


Figure 3. Calculation results of the vdW polaron in monolayer Sb_2O_3 . (a) Band structure of a pristine monolayer $1 \times 1 \text{ Sb}_2\text{O}_3$. The blue and brown dots represent the projections on Sb and O atoms, respectively. The conduction band minimum (CBM) is labeled by the black arrow. Two orange dashed lines denote the energy levels of the valence band maximum (VBM) and CBM. (b) Projected density of states (PDOS) on Sb and O atoms in a pristine monolayer $1 \times 1 \text{ Sb}_2\text{O}_3$. (c) Wave function norm square of the CBM state with an isosurface level of $0.0005 \text{ e}/\text{Bohr}^3$. (d) Illustration of lattice distortions around the vdW polaron. The Sb–O bond length ($d_{\text{Sb-O}}$) and intermolecular distance (d_{inter}) are labeled by black and red dashed lines, respectively. Green arrows indicate the directions that these six Sb_2O_3 molecules aggregate together. (e, f) Projected density of states (PDOS) on six U -treated Sb atoms [(e), labeled by the black dashed circle in (g)] and six Sb atoms far from the polaron [(f), labeled by the purple dashed circle in (g)] in a 5×5 supercell with polaron. The polaronic state is marked by a red arrow in panel (e). (g) Wave function norm square of the polaronic state with an isosurface level of $0.0001 \text{ e}/\text{Bohr}^3$. An effective $U = 7 \text{ eV}$ was applied to the Sb atoms inside the black dashed circle. A purple dashed circle labels Sb atoms far from the polaronic state.

dimensional conductance plot measured across the depressed entity indicates that upon approaching the entity, the CBM shifts continuously toward higher energy, conforming to the decreased entity radius with increasing biases. Concomitantly, on the entity, enhanced density of states (DOS) emerge below -1 V with a peak located at -1.8 V . No differences in electronic properties were observed in the entities residing in different Sb_2O_3 layers.

Our DFT calculations were performed to elucidate the origin of the depressed entities. A plot of the electronic band structures of monolayer Sb_2O_3 is shown in Figure 3a, where

the blue and brown colors represent the contributions from Sb and O atoms to each band, respectively. The emergence of depressed entities after electron irradiation suggests their high relevance to the occupation of empty electronic states of the Sb_2O_3 monolayer with excess electrons. An injected excess electron first partially occupies the empty CBM state of the monolayer. Figure 3c plots the wave function norm square of the CBM state (at the γ point), labeled in Figure 3a,b, which indicates that this state is an intermolecular Sb–Sb bonding state predominantly comprised of Sb p orbitals and primarily located at the interstitial regions among Sb_2O_3 molecules.

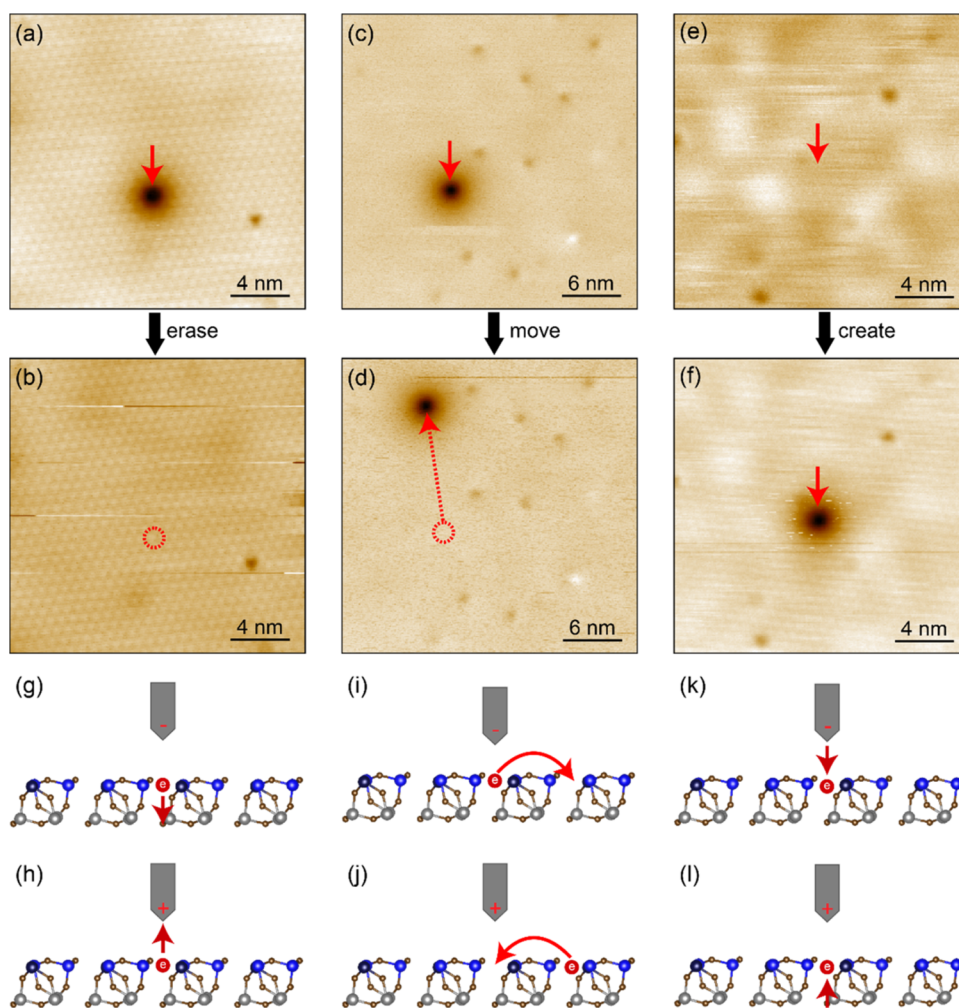


Figure 4. Manipulation of polarons with the STM tip. (a, b) STM images ($V_s = 3$ V, $I_t = 5$ pA) showing the erasure of a polaron. (c, d) STM images ($V_s = 2.5$ V, $I_t = 5$ pA) showing the movement of a polaron. (e, f) STM images ($V_s = 2.8$ V, $I_t = 5$ pA) showing the creation of a polaron. The red dashed circles indicate the initial locations of the polarons before the manipulation. The red arrows indicate the manipulated polarons. The images in (a–f) were taken on the second layer Sb_2O_3 . (g, h) Schematic in (g) [(h)] showing the mechanism of erasure of a polaron at the positive (negative) sample bias [equivalent to the negative (positive) tip bias]. The excess electron is transferred to the substrate (tip), which corresponds to the erasure (g) [(h)] of the polaron. (i, j) Schematic in (i) [(j)] showing the mechanism of movement of a polaron at the positive (negative) sample bias. Under positive (negative) sample bias conditions, the polarons are moved by the tip with repulsive (attractive) forces, respectively. (k, l) Schematic in (k) and [(l)] showing the mechanism of creation of a polaron at the negative (positive) sample bias. The excess electron transfers from the tip (substrate) into Sb_2O_3 and is captured, corresponding to the creation (k) [(l)] of the polaron.

Partial electron occupation of this intermolecular bonding state introduces substantially local lattice distortions to confine the excess electron, which stabilizes it by forming a polaron state through local electron–phonon coupling.

Fully modeling this isolated polaron may require a 10×10 supercell containing 2000 atoms, which is too time-consuming and beyond the typical capability of DFT calculations. As a compromise, we used a 5×5 supercell containing 500 atoms to model the polaron, which is prone to delocalize the polaron state. To ensure that the polaron is localized, an additional U value is added to the p orbitals of those six Sb atoms next to the center site of the polaron (the interstitial site of the Sb_2O_3 monolayer). A U value of 7 eV sufficiently localizes the excess electron in a 5×5 supercell, forming localized polaron. The effects of different U values and different number of treated Sb atoms are discussed in Figures S10 and S11.

To stabilize the excess electron, all six Sb_2O_3 molecules surrounding the excess electron aggregate together that each molecule moves toward the interstitial site by 0.08 \AA [green

arrows in Figure 3d]. Such an aggregation shortens the intermolecular distance (d_{inter}) by 0.13 \AA . Here, distance d_{inter} is defined as the distance between the centers of two molecules, labeled by red dashed lines in Figure 3d. This amount of local lattice distortion is beyond the resolution of our STM measurements. In response to the strengthened intermolecular bonding, the Sb–O bond length of the U -treated Sb ($d_{\text{sb-o}}$), labeled by the black dashed lines in Figure 3d, elongate by $0.06\text{--}0.07 \text{ \AA}$. Consequently, the mechanism of the vdW polaron lies in the electron–phonon coupling of the injected electron and the phonon induced by structural distortion around the interstitial site, as driven by noncovalent interactions. By considering the energy change caused by structural distortions, the formation of the vdW polaron releases a piece of energy by -0.47 eV . Structural distortions of other molecules are negligible (less than 1%).

The formation of this polaron state is highly confined within the excess electron [Figure 3g] and results in a spin-polarized localized polaronic state residing at 0.06 eV below the Fermi

level [Figure 3e]. For comparison, we also plotted the PDOS for a Sb atom (Sb') away from the excess electron in Figure 3f, which is comparable to the PDOS plotted for a Sb atom in the pristine Sb_2O_3 monolayer. Apart from the -0.06 eV polaronic state, the formed polaron nearly maintains the PDOS below the valence band maximum (VBM) and 0.8 eV above the CBM.

Such a polaron formed via intermolecular vdW (non-covalent) interactions is dubbed as a vdW polaron, which is different from conventional polarons, as dictated by ionic or covalent interactions. The vdW polaron substantiates the experimentally observed upward local band bending in Figure 2g, as caused by the localized excess electron. Also, the enhanced DOS below -1 V on the polaron in Figure 2f signifies the polaronic state. We note that the exact energy of the measured polaronic state is typically deeper in energy than the calculated value.²⁶ Thus, the appearance of the polaron state itself is more meaningful than a specific energy level comparable to experimental observation.

We demonstrated the manipulation of polarons with the tip of the STM. Figure 4a,b shows that a polaron can be erased by positioning the STM tip above it and setting the tunneling junction to $+3.5$ V/100 pA for a few seconds. This unambiguously proves its polaron origin instead of crystal defects, as the latter cannot be erased by the tip. Such polaron erasure manipulation can be achieved with both polarity biases but with different threshold values. While the polaron erasure requires positive biases higher than $+3$ V, negative biases as low as -0.5 V already incur the operation. In addition, the polarons can be moved with the tip under both polarity biases using a similar manipulation protocol as the polaron erasure operation but with reduced bias amplitudes. As shown in Figures 4c,d and S12, after placing the tip on top of a polaron with a positive bias of 3 V for a few seconds, the polaron is moved away from the tip, demonstrating a repulsive force acting on the polaron. In contrast, placing the tip adjacent to a polaron with a negative bias of -1.5 V attracts the polaron toward the tip. We found that moving polarons with positive biases has a higher success rate than those with negative biases. Since polarons repel each other, they cannot be moved very close. Moreover, once a polaron forms, additional electrons injected from the tip into the same polaron site experience strong Coulomb repulsions. Thus, only one polaron is created by the tip each time. It is noted that similar polaron manipulation protocol has been developed to an ionic monolayer crystal CoCl_2 ²⁶ whose successful implementation to the current molecular crystal Sb_2O_3 demonstrates its generality.

The polarons can also be created with the tip using both polarity biases. As exemplified in Figure 4e,f, a polaron is created under the tip after setting the tunneling junction at -1.5 V/100 pA for a few seconds. The tip-generated polarons are identical to those generated with electron irradiation, manifesting the same morphology and spectroscopic features [Figure S13]. It is worth mentioning that the success rate of polaron creation is much lower than that of polaron erasure since the former process requires a substantially larger bias amplitude than the latter one, which frequently destroys the weakly vdW-bonded Sb_2O_3 films.

Having developed the protocol for polaron manipulation, we investigated the physical mechanism of those processes. Different polaron manipulations, including erasure, creation, and movement, correspond to different charge transfer

processes for excess electrons. Namely, erasing (creating) a polaron is accompanied by transferring an electron to (from) the tip or substrate from (into) the Sb_2O_3 film, as schematically shown in Figure 4g,h [Figure 4k,l]. Moving a polaron is associated with the hopping of the polaron among equivalent occupation sites within the film [Figure 4i,j].

The above experiments demonstrated that the polarons are moved with repulsive/attractive forces by the tip under positive/negative sample bias conditions, respectively. This observation suggests that the electric field generated from the tip E_{tip} provides the driving force for the polaron movement. For the processes of polaron creation (erasure), the excess electron may overcome an energy barrier to get trapped (released) into (from) the Sb_2O_3 film, which requires an inelastic electron tunneling process to overcome the energy barrier. To evaluate such a scenario, we examined the relationship of voltage and the probability of erasing polarons, a process that is mostly controllable.

For that, statistical analyses for the success rate of polaron erasure as a function of sample bias were performed at both polarity biases. Here, the success rate is defined as the ratio between the number of successfully erased polarons and the total number of manipulated polarons for erasure (about 20) over the same duration time of 10 s. To ensure each erasure manipulation has the identical initial tip height Z_0 , the tunneling junction is first set at 3 V/100 pA (-1 V/10 pA) in the clean Sb_2O_3 region for the erasure with positive (negative) bias. Then, the tip is moved on top of polarons with a disabled feedback loop, and the tunneling current is recorded ever since. As shown in Figure 5a [Figure 5c], the tunneling current jumps from the low (high) to high (low) state, signifying that the polaron is successfully erased with positive

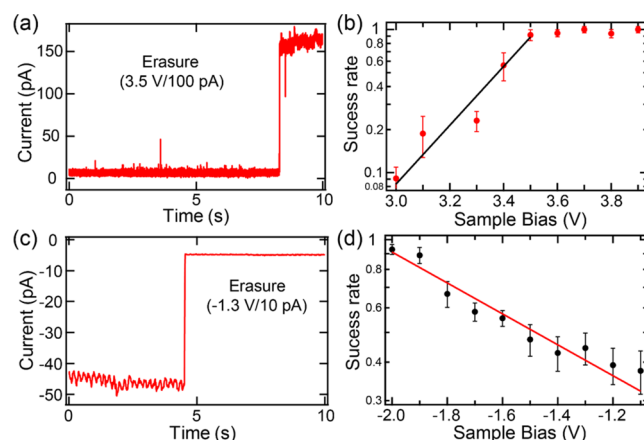


Figure 5. Mechanism for the erasure of polarons. (a, b) To ensure a consistent initial tip height Z_0 , it is set to 3 V/100 pA in the clean area. Next, the sample bias is modulated to a specific value with the feedback loop off, and then the tip is moved above the polaron, after which the current change is immediately recorded within 10 s. A current jump from a low current state to a high current state has been recorded at 3.5 V, as indicated in panel (a). Using this approach, the statistics of the polarons erasure rate at different sample biases (3.0 to 3.9 V) are presented in panel (b). The black line is a fitting to the data below 3.5 V with an exponential relation. (c, d) Similar as (a, b), but the initial tip height Z_0 is set to -1 V/10 pA, and a current jump from the high current state to a low current state has been recorded at -1.3 V in (c). The statistical sample bias in (d) ranges from -1.1 to -2.0 V. The red line is also a fitting to the data with an exponential relation. Note that the data in (b, d) are plotted in logarithmic coordinates.

(negative) bias. Statistics in Figure 5b [Figure 5d] indicate that the success rate of polaron erasure increases exponentially with increasing bias amplitude and eventually saturates to nearly unity above 3.5 V (below -2 V) for positive (negative) biases. This justifies that the mechanism behind the polaron erasure is determined by an inelastic electron tunneling effect.^{6,19,42}

CONCLUSIONS

In summary, we investigated the excess electrons residing in polarons of ultrathin molecular crystal Sb_2O_3 that were grown with MBE. Our STM measurements resolved the interstitial occupation sites of the polarons, exhibiting pertinent local band bending and polaronic states. As elucidated from DFT calculations, such a polaron is an intermolecular vdW polaron. Its excess electron is confined in a region with locally shortened intermolecular distances, wherein the vdW interactions dominate the intermolecular distances. We showed the creation of large ensembles of polarons with controlled electron beam irradiations, as well as the manipulation of single polarons individually, including creation, erasure, and lateral movement. While the tip electric field provides the driving force for the polaron movement, the inelastic electron tunneling effect leads to the polaron erasure. Our study demonstrates the feasibility of manipulating single electrons hosted by intermolecular vdW polarons, enriching the polaron systems and setting the basis for tailoring chemical processes via polarons. Given the tremendous progress of utilizing molecular crystals as dielectric layers,^{40,43} our study opens up the possibility of fabricating polaron devices based on these dielectric layers themselves.

METHODS

Experiment. The $\alpha\text{-Sb}_2\text{O}_3$ thin films were prepared on a graphene-covered SiC(0001) substrate by molecular-beam epitaxy. The detailed procedures for preparing the graphene substrate have been reported in ref 44. High-purity Sb_2O_3 powder (1–3 mm in diameter, 99.999%) is evaporated at about 570 K from a homemade crucible, and the substrate temperature is kept around 370 K during the sample growth. The base pressure is better than 7×10^{-9} Torr.

When irradiating the Sb_2O_3 films with an electron beam, a voltage of 3 V was applied to the filament, and the sample was kept at a large distance of about 20 cm away from the filament without any acceleration voltage between them. Our filament temperature was estimated as ~ 2600 K, corresponding to a mean kinetic energy of ~ 0.45 eV for the emitted hot electrons.⁴⁵ Therefore, instead of generating electron–hole pairs by high-voltage electron beam irradiation reported previously,⁴⁶ merely low-energy electrons were injected into the Sb_2O_3 films in our case. To avoid possible contamination to the film, the sample was postannealed at the growth temperature of 370 K. Such a low temperature is still insufficient for the excess electrons to escape the polaron trapping potential.

STM/STS measurements were conducted in custom-designed cryogenic Unisoku STM systems (1500) at 4.2 K. An electrochemically etched W wire was used as the STM tip, which had been characterized on the Ag(111) surface prior to the measurements. The STS was taken using a standard lock-in technique with a bias modulation at 983 Hz.

First-Principles Calculations. Density functional theory calculations were performed using the generalized gradient approximation for the exchange–correlation potential, employing the projector augmented wave method^{47,48} and a plane-wave basis set as implemented in the Vienna Ab Initio Simulation Package (VASP).⁴⁹ For the structural relaxation and electronic property calculations, Grimme's D3 form of van der Waals correction was applied, along with the Perdew Burke Ernzerhof (PBE) exchange

functional (PBE-D3).^{50,51} Geometric properties of the Sb_2O_3 unit cell were computed using a 700 eV cutoff kinetic energy and a $9 \times 9 \times 1$ k-mesh. The lattice constant was fully relaxed, until the residual force per atom was less than 0.01 eV/Å. A vacuum layer of approximately 17 Å was included in the calculations to avoid the interlayer interaction. The band structure of the monolayer was also revealed using the HSE functional, which exhibits similar shapes and dispersions of electronic bands near the bandgap but shows an over 1 eV larger bandgap value, as shown in Figure S14. To simulate the polarons, a $5 \times 5 \times 1$ supercell with a fixed lattice constant was employed, and structure optimization and electronic structure calculations were performed using a kinetic energy cutoff of 350 eV and a single Γ point. To account for the on-site Coulomb interaction with the Sb *p* orbital in the polaron region, a *U* value of 7 eV is adopted for the six Sb atoms around the interstitial site of the polaron. The detailed discussions regarding the *U* parameters are presented in Figures S10 and S11.

ASSOCIATED CONTENT

Supporting Information

The Supporting Information is available free of charge at <https://pubs.acs.org/doi/10.1021/jacs.4c04450>.

More detailed STM experimental data on Sb_2O_3 thin films; various moiré patterns on Sb_2O_3 thin films; atomic force microscopy measurements; additional STM experimental measurements on the polaron; another type of polaron on Sb_2O_3 thin films, and additional theoretical calculation (PDF)

AUTHOR INFORMATION

Corresponding Authors

Wei Ji – Beijing Key Laboratory of Optoelectronic Functional Materials & Micro-Nano Devices, Department of Physics, Renmin University of China, Beijing 100872, China; Key Laboratory of Quantum State Construction and Manipulation (Ministry of Education), Renmin University of China, Beijing 100872, China; orcid.org/0000-0001-5249-6624; Email: wji@ruc.edu.cn

Ying-Shuang Fu – School of Physics and Wuhan National High Magnetic Field Center, Huazhong University of Science and Technology, Wuhan 430074, China; Wuhan Institute of Quantum Technology, Wuhan 430206, China; orcid.org/0000-0001-7876-2812; Email: yfu@hust.edu.cn

Authors

Zhi-Hao Zhang – School of Physics and Wuhan National High Magnetic Field Center, Huazhong University of Science and Technology, Wuhan 430074, China

Linlu Wu – Beijing Key Laboratory of Optoelectronic Functional Materials & Micro-Nano Devices, Department of Physics, Renmin University of China, Beijing 100872, China; Key Laboratory of Quantum State Construction and Manipulation (Ministry of Education), Renmin University of China, Beijing 100872, China

Mao-Peng Miao – School of Physics and Wuhan National High Magnetic Field Center, Huazhong University of Science and Technology, Wuhan 430074, China

Hao-Jun Qin – School of Physics and Wuhan National High Magnetic Field Center, Huazhong University of Science and Technology, Wuhan 430074, China

Gang Chen – School of Physics and Wuhan National High Magnetic Field Center, Huazhong University of Science and Technology, Wuhan 430074, China

Min Cai – School of Physics and Wuhan National High Magnetic Field Center, Huazhong University of Science and Technology, Wuhan 430074, China

Lixin Liu – State Key Laboratory of Material Processing and Die & Mould Technology, School of Materials Science and Engineering, Huazhong University of Science and Technology, Wuhan 430074, China

Lan-Fang Zhu – School of Physics and Wuhan National High Magnetic Field Center, Huazhong University of Science and Technology, Wuhan 430074, China

Wenhao Zhang – School of Physics and Wuhan National High Magnetic Field Center, Huazhong University of Science and Technology, Wuhan 430074, China; orcid.org/0000-0003-2386-0305

Tianyou Zhai – State Key Laboratory of Material Processing and Die & Mould Technology, School of Materials Science and Engineering, Huazhong University of Science and Technology, Wuhan 430074, China; orcid.org/0000-0003-0985-4806

Complete contact information is available at:
<https://pubs.acs.org/10.1021/jacs.4c04450>

Author Contributions

#Z.-H.Z. and L.W. contributed equally to this work.

Notes

The authors declare no competing financial interest.

ACKNOWLEDGMENTS

This work was funded by the National Key Research and Development Program of China (Grant No. 2022YFA1402400) and the National Natural Science Foundation of China (Grant Nos. U20A6002, 92265201, 12047508, 11974422). W.J. gratefully acknowledges financial support from the Ministry of Science and Technology of China (Grant No. 2018YFE0202700), Strategic Priority Research Program of the Chinese Academy of Sciences (Grant No. XDB30000000), Fundamental Research Funds for the Central Universities, and Research Funds of Renmin University of China (Grant No. 22XNKJ30). L.L.W. was supported by the Outstanding Innovative Talents Cultivation Funded Programs 2022 of Renmin University of China. Calculations were performed at the Physics Lab of High-Performance Computing of Renmin University of China, Shanghai Supercomputer Center.

REFERENCES

- (1) Otero, R.; Rosei, F.; Besenbacher, F.; et al. Scanning tunneling microscopy manipulation of complex organic molecules on solid surfaces. *Annu. Rev. Phys. Chem.* **2006**, *57*, 497–525.
- (2) Morgenstern, K.; Lorente, N.; Rieder, K. H.; et al. Controlled manipulation of single atoms and small molecules using the scanning tunnelling microscope. *Phys. Status Solidi (B)* **2013**, *250*, 1671–1751.
- (3) Khajetoorians, A. A.; Wegner, D.; Otte, A. F.; et al. Creating designer quantum states of matter atom-by-atom. *Nat. Rev. Phys.* **2019**, *1*, 703–715.
- (4) Hla, S. W. Atom-by-atom assembly. *Rep. Prog. Phys.* **2014**, *77*, No. 056502.
- (5) Coropceanu, V.; Cornil, J.; da Silva Filho, D. A.; et al. Charge Transport in Organic Semiconductors. *Chem. Rev.* **2007**, *107*, 926–952.
- (6) Repp, J.; Meyer, G.; Olsson, F. E.; et al. Controlling the Charge State of Individual Gold Adatoms. *Science* **2004**, *305*, 493–495.
- (7) Wu, S. W.; Ogawa, N.; Ho, W.; et al. Atomic-Scale Coupling of Photons to Single-Molecule Junctions. *Science* **2006**, *312*, 1362–1365.

(8) Scheuerer, P.; Patera, L. L.; Simbürger, F.; et al. Charge-Induced Structural Changes in a Single Molecule Investigated by Atomic Force Microscopy. *Phys. Rev. Lett.* **2019**, *123*, No. 066001.

(9) Teichmann, K.; Wenderoth, M.; Loth, S.; et al. Controlled Charge Switching on a Single Donor with a Scanning Tunneling Microscope. *Phys. Rev. Lett.* **2008**, *101*, No. 076103.

(10) Gou, J.; Xia, B.; Wang, X.; et al. Realizing quinary charge states of solitary defects in two-dimensional intermetallic semiconductor. *Natl. Sci. Rev.* **2022**, *9*, No. nwab070.

(11) Li, H.; Li, S.; Naik, M. H.; et al. Imaging local discharge cascades for correlated electrons in WS₂/WSe₂ moiré superlattices. *Nat. Phys.* **2021**, *17*, 1114–1119.

(12) Landau, L. D. On the motion of electrons in a crystal lattice. *Phys. Z. Sowjetunion* **1933**, *3*, No. 664.

(13) Pekar, S. Local quantum states of electrons in an ideal ion crystal. *J. Exp. Theor. Phys.* **1946**, *16*, 341–348.

(14) Fröhlich, H. Electrons in lattice fields. *Adv. Phys.* **1954**, *3*, 325–361.

(15) Holstein, T. Studies of polaron motion: Part II. The “small” polaron. *Ann. Phys.* **1959**, *8*, 343–389.

(16) Franchini, C.; Reticcioli, M.; Setvin, M.; et al. Polarons in materials. *Nat. Rev. Mater.* **2021**, *6*, 560–586.

(17) Natanzon, Y.; Azulay, A.; Amouyal, Y.; et al. Evaluation of Polaron Transport in Solids from First-principles. *Isr. J. Chem.* **2020**, *60*, 768–786.

(18) Papageorgiou, A. C.; Beglitis, N. S.; Pang, C. L.; et al. Electron traps and their effect on the surface chemistry of TiO₂(110). *Proc. Natl. Acad. Sci. U.S.A.* **2010**, *107*, 2391–2396.

(19) Di Valentin, C.; Pacchioni, G.; Selloni, A.; et al. Reduced and n-Type Doped TiO₂: Nature of Ti³⁺ Species. *J. Phys. Chem. C* **2009**, *113*, 20543–20552.

(20) Reticcioli, M.; Sokolović, I.; Schmid, M.; et al. Interplay between Adsorbates and Polarons: CO on Rutile TiO₂(110). *Phys. Rev. Lett.* **2019**, *122*, No. 016805.

(21) Yim, C. M.; Chen, J.; Zhang, Y.; et al. Visualization of Water-Induced Surface Segregation of Polarons on Rutile TiO₂(110). *J. Phys. Chem. Lett.* **2018**, *9*, 4865–4871.

(22) Ren, Z.; Shi, Z.; Feng, H.; et al. Recent Progresses of Polarons: Fundamentals and Roles in Photocatalysis and Photoelectrocatalysis. *Adv. Sci.* **2023**, No. 2305139.

(23) Setvin, M.; Franchini, C.; Hao, X.; et al. Direct View at Excess Electrons in TiO₂ Rutile and Anatase. *Phys. Rev. Lett.* **2014**, *113*, No. 086402.

(24) Guo, C.; Meng, X.; Fu, H.; et al. Probing Nonequilibrium Dynamics of Photoexcited Polarons on a Metal-Oxide Surface with Atomic Precision. *Phys. Rev. Lett.* **2020**, *124*, No. 206801.

(25) Chen, C.; Avila, J.; Frantzeskakis, E.; et al. Observation of a two-dimensional liquid of Fröhlich polarons at the bare SrTiO₃ surface. *Nat. Commun.* **2015**, *6*, No. 8585.

(26) Cai, M.; Miao, M. P.; Liang, Y.; et al. Manipulating single excess electrons in monolayer transition metal dihalide. *Nat. Commun.* **2023**, *14*, No. 3691.

(27) Liu, H.; Wang, A.; Zhang, P.; et al. Atomic-scale manipulation of single-polaron in a two-dimensional semiconductor. *Nat. Commun.* **2023**, *14*, No. 3690.

(28) Wang, F.; Fu, Y.; Ziffer, M. E.; et al. Solvated Electrons in Solids—Ferroelectric Large Polarons in Lead Halide Perovskites. *J. Am. Chem. Soc.* **2021**, *143*, 5–16.

(29) Tao, W.; Zhang, C.; Zhou, Q.; et al. Momentarily trapped exciton polaron in two-dimensional lead halide perovskites. *Nat. Commun.* **2021**, *12*, No. 1400.

(30) Ghosh, R.; Spano, F. C.; et al. Excitons and Polarons in Organic Materials. *Acc. Chem. Res.* **2020**, *53*, 2201–2211.

(31) Nightingale, J.; Wade, J.; Moia, D.; et al. Impact of Molecular Order on Polaron Formation in Conjugated Polymers. *J. Phys. Chem. C* **2018**, *122*, 29129–29140.

(32) Qiao, J.; Kong, X.; Hu, Z. X.; et al. High-mobility transport anisotropy and linear dichroism in few-layer black phosphorus. *Nat. Commun.* **2014**, *5*, No. 4475.

- (33) Cui, X.; Han, D.; Guo, H.; et al. Realizing nearly-free-electron like conduction band in a molecular film through mediating intermolecular van der Waals interactions. *Nat. Commun.* **2019**, *10*, No. 3374.
- (34) Xing, S.; Wu, L.; Wang, Z.; et al. Interweaving Polar Charge Orders in a Layered Metallic Superatomic Crystal. *Phys. Rev. X* **2022**, *12*, No. 041034.
- (35) Qiao, J.; Pan, Y.; Yang, F.; et al. Few-layer Tellurium: one-dimensional-like layered elementary semiconductor with striking physical properties. *Sci. Bull.* **2018**, *63*, 159–168.
- (36) Xian, J.-J.; Wang, C.; Nie, J. H.; et al. Spin mapping of intralayer antiferromagnetism and field-induced spin reorientation in monolayer CrTe₂. *Nat. Commun.* **2022**, *13*, No. 257.
- (37) Grzechnik, A. Compressibility and Vibrational Modes in Solid As₄O₆. *J. Solid State Chem.* **1999**, *144*, 416–422.
- (38) Han, W.; Huang, P.; Li, L.; et al. Two-dimensional inorganic molecular crystals. *Nat. Commun.* **2019**, *10*, No. 4728.
- (39) Liu, K.; Jin, B.; Han, W.; et al. A wafer-scale van der Waals dielectric made from an inorganic molecular crystal film. *Nat. Electron.* **2021**, *4*, 906–913.
- (40) Svensson, C. Refinement of the crystal structure of cubic antimony trioxide, Sb₂O₃. *Acta Crystallogr., Sect. B: Struct. Crystallogr. Cryst. Chem.* **1975**, *31*, 2016–2018.
- (41) Peng, J.; Pu, W.; Lu, S.; et al. Inorganic Low k Cage-molecular Crystals. *Nano Lett.* **2021**, *21*, 203–208.
- (42) Liljeroth, P.; Repp, J.; Meyer, G. Current-Induced Hydrogen Tautomerization and Conductance Switching of Naphthalocyanine Molecules. *Science* **2007**, *317*, 1203–1206.
- (43) Xu, Y.; Liu, T.; Liu, K.; et al. Scalable integration of hybrid high- κ dielectric materials on two-dimensional semiconductors. *Nat. Mater.* **2023**, *22*, 1078–1084.
- (44) Yang, X.; Xian, J. J.; Li, G.; et al. Possible Phason-Polaron Effect on Purely One-Dimensional Charge Order of Mo₆Se₆ Nanowires. *Phys. Rev. X* **2020**, *10*, No. 031061.
- (45) Jones, J. H. The kinetic energy of electrons emitted from a hot tungsten filament. *Proc. R. Soc. London, Ser. A* **1923**, *102*, 734–751.
- (46) Zhang, Z.; Yates, J. T.; et al. Direct Observation of Surface-Mediated Electron-Hole Pair Recombination in TiO₂(110). *J. Phys. Chem. C* **2010**, *114*, 3098–3101.
- (47) Blöchl, P. E. Projector augmented-wave method. *Phys. Rev. B* **1994**, *50*, No. 17953.
- (48) Kresse, G.; Joubert, D.; et al. From ultrasoft pseudopotentials to the projector augmented-wave method. *Phys. Rev. B* **1999**, *59*, No. 1758.
- (49) Kresse, G.; Furthmüller, J.; et al. Efficient iterative schemes for ab initio total-energy calculations using a plane-wave basis set. *Phys. Rev. B* **1996**, *54*, No. 11169.
- (50) Grimme, S.; Antony, J.; Ehrlich, S.; et al. A consistent and accurate ab initio parametrization of density functional dispersion correction (DFT-D) for the 94 elements H-Pu. *J. Chem. Phys.* **2010**, *132*, No. 154104.
- (51) Perdew, J. P.; Burke, K.; Ernzerhof, M.; et al. Generalized Gradient Approximation Made Simple. *Phys. Rev. Lett.* **1996**, *77*, No. 3865.